

Time-resolved measurement of single electrons using a modulated barrier

Wanki Park^{1*†}, Chanuk Yang^{2,3†}, Young-Seok Ghee¹, Hyung Kook Choi³, Bum-Kyu Kim¹ and Myung-Ho Bae^{1,4*}

¹Korea Research Institute of Standards and Science, Daejeon 34113, Republic of Korea

²Jeonbuk National University G-LAMP Project Group, Jeonbuk National University, Jeonju 54896, Republic of Korea

³Department of Physics, Jeonbuk National University, Jeonju 54896, Republic of Korea

⁴KAIST Graduate School of Quantum Science and Technology, Korea Advanced Institute of Science and Technology, Daejeon 34141, Republic of Korea

†W.P. and C.Y. contributed equally to this work.

*e-mail: wanki@kriss.re.kr, mhbae@kriss.re.kr

Abstract

Measuring the wave packet of high-energy electrons in solid-state devices is important for quantum information processing. Time-resolved measurements with high time resolutions and small errors typically require detectors with a large RF bandwidth. Here, we demonstrate a precise and time-efficient time-resolved method, where an accuracy in measurements are not limited by the bandwidth. By analyzing the energy variance derived from transconductance measurements under a sinusoidal gate voltage applied to a detector barrier, we extract key characteristics of single-electron states. It includes a temporal variance and the covariance between energy and time. The results are consistent with those obtained using a hyperbolic tangent shaped (linearly varying) gate voltage. The proposed approach provides a simple yet precise method for probing the single-electron states. The present findings will be useful for identifying suitable waveforms for applications in electron quantum optics and quantum information processing.

Introduction

Single electrons in a two-dimensional electron gas (2DEG) system have been generated via several methods, including time-varying modulations of a mesoscopic capacitor ¹, electrical contact ^{2, 3}, and interacting quantum dots (quantum dot pump) ^{4, 5, 6, 7}, and surface acoustic waves ^{8, 9}. The generated electrons are used in applications such as electron quantum optics ^{3, 10, 11} and quantum information processing ^{12, 13}. A crucial step applying such system is determining the quantum states of the generated electrons, which enables verification of the prescribed states and probing of the suitability of the generated electrons for applications. Various techniques have been used to characterize the state of generated electrons, differing based on the emission energy of the generated electrons.

For low-energy electrons such as those generated from electrical contacts or mesoscopic capacitors, the quantum state is measured using Hong-Ou-Mandel type collisions with a reference Fermi sea ^{14, 15, 16}. By modulating the Fermi sea with a sinusoidal voltage and analyzing shot noise ^{15, 16}, one can probe the density matrix of electron wave functions. The arrival time distribution of generated electrons can be measured using a current detector ¹. Bandwidth limitations of the detector, however, make it difficult to achieve picosecond resolution.

For hot electrons far above the Fermi energy, such as those generated by a quantum dot pump, the electron states are measured using a potential (detector) barrier that acts as an energy filter. This filter allows only single electrons with energies above the barrier height to pass. Hence, by measuring the transmission current while tuning the static barrier height, the energy distribution of single electrons can be extracted ¹⁷. An arrival time distribution can be obtained by applying an AC voltage to the barrier ^{17, 18}. For accurate measurement, this method requires fast ramping¹⁹ of the barrier, necessitating a high bandwidth of the RF line controlling the barrier. Tomographic measurements have been demonstrated by collecting current distributions while varying the rate of change of the barrier height ^{20, 21, 22}. By using the inverse Radon transformation, Wigner distributions ^{20, 23} of electrons are reconstructed, providing a phase-space representation related to the density matrix. This method also requires a RF signal with a high bandwidth, particularly for large tomographic angles.

In this paper, we present a method for extracting the temporal variance and the covariance between energy and time of electrons without fully reconstructing the arrival time distribution

or Wigner distributions. By applying a sinusoidal gate voltage to the detector barrier, we obtain the transconductance (the derivative of the transmitted current with respect to the barrier height) as a function of the time delay between pumping and detecting. Using the variance of the barrier height in the transconductance, we extract the temporal variance and the covariance between energy and time. Our findings show that time-resolved measurements of electron temporal widths as short as ~ 17 picoseconds can be achieved using a 240 MHz sinusoidal gate voltage, which corresponds to a period of ~ 4 nanoseconds. We validate the results obtained using the sinusoidal gate voltage by comparing them with those obtained using a hyperbolic tangent shaped voltage, which generates linearly varying time profiles and has been typically used in previous tomographic measurements^{20,24}.

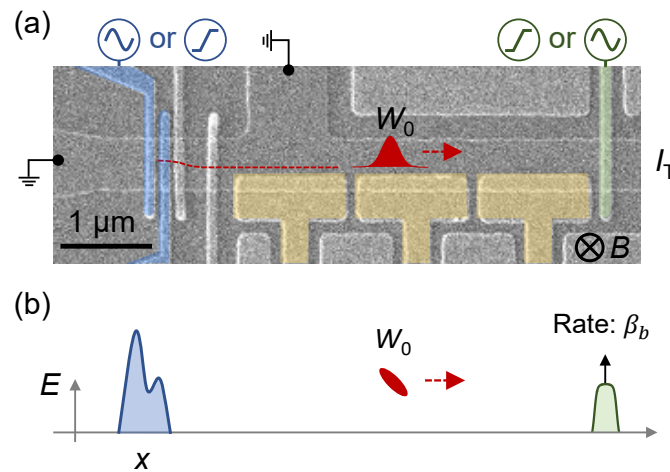


Figure 1. (a) Experimental setup. The quantum dot (blue region) is modulated over time by a sinusoidal gate voltage, producing single electrons periodically. W_0 represents the Wigner distribution of the generated electrons. To perform time-resolved measurements, the detector potential barrier (green region) is also modulated periodically. The distance between the quantum dot and the detector potential barrier is $\sim 5 \mu\text{m}$. Scale bar: $1 \mu\text{m}$. (b) Schematic representation of the setup with respect to position and energy.

Results

Experimental setup

Our experimental demonstration is conducted in a 2DEG formed in a GaAs/AlGaAs

heterostructure (see the Method for detail). The experimental setup is shown schematically in Figs. 1(a) and 1(b). For single-electron generation, we modulate a quantum dot (blue region) over time using either sinusoidal or trapezoidal waveforms with a pumping frequency of f_p . The trapezoidal waveform is linear over time during emission, and is a convenient way of altering emission distributions by varying f_p . The pumping generates single electrons with a pumping current of ef_p and an emission energy ~ 100 meV above the Fermi energy¹⁷. Here, e is the elementary charge. The generated single electrons, characterized by a Wigner distribution W_0 , propagate through the quantum Hall channel under a perpendicular magnetic field of $B = 12$ T. Side gates [yellow regions in Fig. 1(a)] with negative gate voltages are introduced to suppress the emission of longitudinal optical (LO) phonons of electrons during propagation through the quantum Hall channel²⁵.

To perform time-resolved measurements of the generated electrons, we apply a sinusoidal gate voltage $V_b(t) = V_{AC} \sin 2\pi f_b(t - t_d) + V_{DC}$ (where t_d denotes the time delay to the pumping) to the detector barrier [formed by the green gate in Fig. 1(a)], and measure the transmitted current of electrons through the barrier (I_T). In our experimental regime, the AC period $1/f_b$ (~ 4 ns for $f_b = 240$ MHz) is much larger than the temporal width of incident (generated) electrons (≤ 30 ps)²⁰ and the traversal time of electrons through the barrier (≤ 10 ps)¹⁹. Under this condition, a rate β_b of change of the barrier over time, around the arrival time of electrons at the barrier, can be described as linear. This rate is related with the gate voltage as $\beta_b \simeq -\alpha_b \partial V_b / \partial t|_{t=\langle t \rangle_b}$, where $\langle t \rangle_b$ is the mean arrival time of electrons at the barrier and α_b is the conversion factor from the gate voltage to the barrier height. The factor α_b can be obtained from LO phonon replicas in energy measurements²⁶. For the sinusoidal voltage, this rate depends both on the AC amplitude and the time delay t_d .

We also consider the case where the gate voltage V_b has the hyperbolic tangent shape $V_b(t) = V_{AC} \tanh[A \sin[2\pi f_b(t - t_d)]] + V_{DC}$, which is frequently used for obtaining arrival time distribution and tomographic measurements^{20, 22}. In this waveform, varying A alters the rate β_b . We demonstrate that the hyperbolic tangent shape yields consistent with those obtained using sinusoidal modulation.

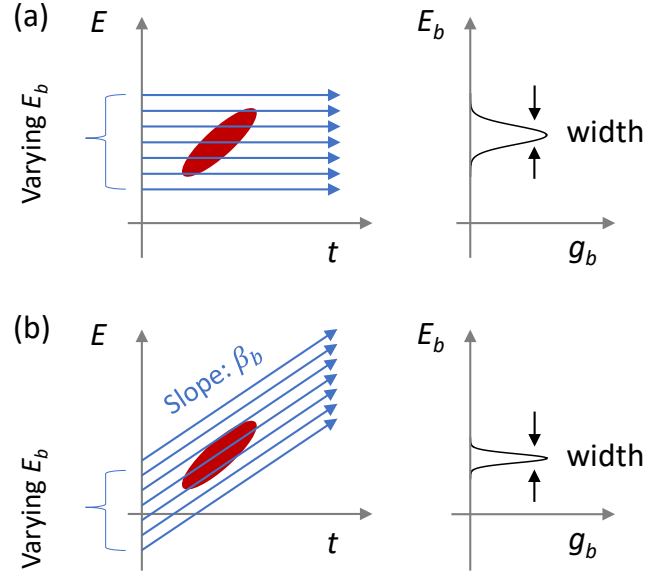


Figure 2. (a,b) Wigner distributions (red ovals) are shown in the energy-time phase space at the left panels. The projected distributions along the blue arrows are shown in right panels. The projected distribution is equivalent to the transconductance g_b when the energy window of the potential barrier is negligible. They are shown for (a) a static barrier and (b) a barrier height linearly modulated with a rate β_b .

Parameter extraction using transconductance

Hot electrons have been measured using the transconductance of the current through the detector barrier^{17, 18, 20}. We define the (normalized) transconductance g_b as

$$g_b \equiv -\frac{1}{ef_p} \frac{\partial I_T}{\partial E_b},$$

where ef_p is the pumping current used to normalize the current, and $E_b \equiv -\alpha_b V_{DC}$ denotes the DC component of the barrier height controlled by V_{DC} . Under a linearized barrier height rate β_b for a given t_d , the transconductance g_b is expressed as²¹

$$g_b = -\frac{\partial}{\partial E_b} \left[\int_{-\infty}^{\infty} dt \int_{-\infty}^{\infty} dE W_0(E, t) T(E - E_b - \beta_b t + \text{const}) \right], \quad (1)$$

where W_0 is the Wigner distribution of the incident (generated) electrons, const denotes a factor independent of the energy E and time t , and T is an energy-dependent transmission probability of monochromatic electrons through the detector barrier in the absence of the AC voltage.

For the static potential barrier ($\beta_b = 0$), the barrier acts as an energy filter¹⁷ allowing a part of electrons whose energy exceeds the barrier height (treating T as a step function). Then Eq. (1) approximates the projection of the incident Wigner distribution W_0 onto the energy space. This yields the energy distribution of electrons [shown in Fig. 2(a)]. For a finite β_b , Eq. (1) approximates the projection of W_0 onto the energy space along tilted lines^{19, 21} with slope β_b [as shown in Fig. 2(b)]. The projected distribution depends on both the barrier height rate β_b and the detailed shape of W_0 .

We examine the variance in the barrier height (corresponding to the energy scale) while electrons travels across the barrier, $\langle \Delta E_b^2 \rangle_g \equiv \langle E_b^2 \rangle_g - \langle E_b \rangle_g^2$ for a given rate β_b , where $\langle E_b^k \rangle_g \equiv \int_{-\infty}^{\infty} dE_b E_b^k g_b$. This variance of the barrier height can be computed as (see Supplementary Note 1 for detail),

$$\langle \Delta E_b^2 \rangle_g = \langle \Delta E^2 \rangle_0 + \Delta_b^2 - 2\beta_b (\langle Et \rangle_0 - \langle E \rangle_0 \langle t \rangle_0) + \beta_b^2 \langle \Delta t^2 \rangle_0, \quad (2)$$

where $\langle O \rangle_0 \equiv \int_{-\infty}^{\infty} dE dt O W_0$ and Δ_b is the energy width (the standard deviation) of $\partial T / \partial E$, accounting for errors in measurements due to tunneling effects. Equation (2) is a key result of this study. The coefficient multiplying β_b^2 corresponds to the temporal variance $\langle \Delta t^2 \rangle_0$, while the coefficient multiplying $-2\beta_b$ corresponds to the covariance between energy and time, $\langle Et \rangle_0 - \langle E \rangle_0 \langle t \rangle_0$. Importantly, this extraction does not depend on detailed shape of dT/dE_b and the constant term in Eq. (1). The barrier height variance at $\beta_b = 0$ [the constant term, independent of β_b in Eq. (2)] approximates the energy variance $\langle \Delta E^2 \rangle_0$ of the incident electrons¹⁷ when Δ_b is negligible. By obtaining Eq. (2) as a function of β_b , we demonstrate the extraction of these parameters.

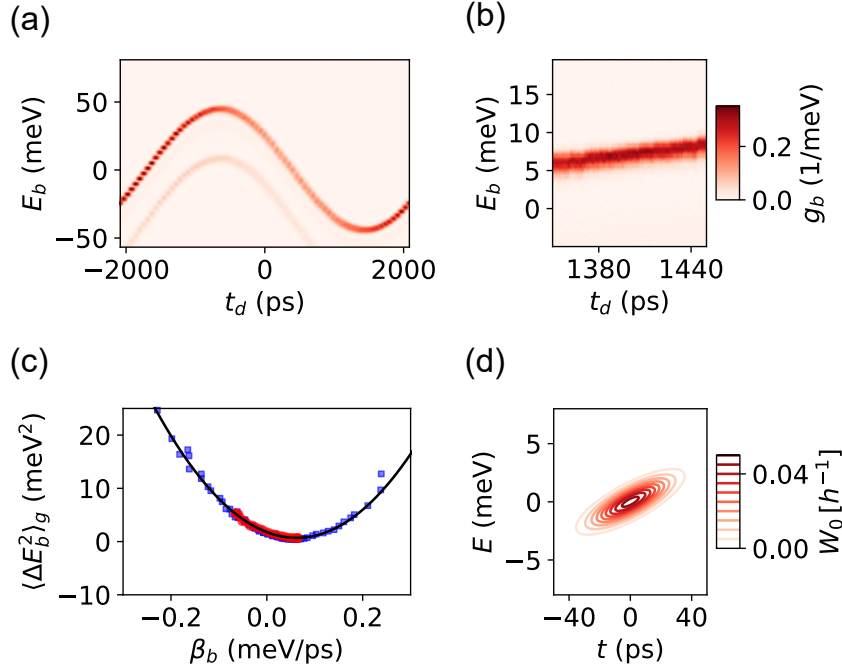


Figure 3. Measurements with sinusoidal pumping at $f_p = 240$ MHz. (a,b) The transconductance g_b as a function of t_d and E_b with (a) a sinusoidal and (b) a hyperbolic tangent shaped waveform applied to the detector barrier. In (a), $V_{AC} = 82$ mV and $f_b = 240$ MHz are used and β_b varies from -0.07 to 0.07 meV/ps. In (b), g_b is shown for $\beta_b = 0.023$ meV/ps with $f_b = 2.4$ GHz is shown. (c) The barrier height variance $\langle \Delta E_b^2 \rangle_g$ obtained from g_b with the sinusoidal wave [from (a)] is shown as red circles, fitted to Eq. (2) (the black solid curve). $\langle \Delta E_b^2 \rangle_g$ obtained from g_b with the hyperbolic tangent wave [as in (b)] is shown as blue rectangles. (d) The Wigner distribution of generated electrons is illustrated, assuming that the generated electrons are described by a bivariate Gaussian Wigner distribution with the parameters obtained in (c). h denotes the Planck constant.

Experimental demonstration

Figure 3(a) shows the transconductance g_b as a function of t_d (hence varying β_b) and E_b , measured while applying a sinusoidal waveform to the detector barrier with a frequency $f_b = 240$ MHz and $V_{AC} = 82$ mV. The same frequency, $f_p = 240$ MHz, is used for single-electron pumping. The high-energy curve (with larger intensity) is produced by electrons that do not experience LO phonon emission on the way to the detector, while the low-energy curve (with lower intensity) corresponds to electrons that undergo one LO phonon emission. The high energy curve is used for measuring the state of incident electrons, and, by determining the gate voltage between the two curves, the conversion factor $\alpha_b = 0.54$ eV/V is obtained²⁶.

It is observed that varying t_d alters the barrier height rate β_b (the slope of the curve) and the corresponding barrier height variance. This variation is attributed to the time-energy filtering of electrons, as shown in Fig. 2. For given $V_{AC} = 82$ mV and $f_b = 240$ MHz in Fig. 3, β_b ranges from -0.07 to 0.07 meV/ps. To demonstrate consistency with the results obtained using the hyperbolic tangent shaped waveform, we apply this waveform to the detector barrier at $f_b = 2.4$ GHz and vary β_b by adjusting A . As an example, the variation in g_b as a function of t_d and E_b for $\beta_b = 0.023$ meV/ps is shown in Fig. 3(b).

From the transconductance g_b in Figs. 3(a) and 3(b), we obtain the variance $\langle \Delta E_b^2 \rangle_g$ as a function of β_b [Fig. 3(c)] (see the Method for extraction of the variance and β_b). The results for the sinusoidal waveform [Fig. 3(a)] are shown as red circles. These are well-fitted to Eq. (2) (black solid curve), from which we extract $\langle \Delta t^2 \rangle_0 = (16.7 \text{ ps})^2$ and $\langle Et \rangle_0 - \langle E \rangle_0 \langle t \rangle_0 = 17.4 \text{ meV} \cdot \text{ps}$, and assuming that Δ_b^2 is negligible, we estimate $\langle \Delta E^2 \rangle_0 \simeq (1.33 \text{ meV})^2$ (see Method for the extraction). The correlation coefficient is found to be 0.78, which is the normalized value of the covariance with the product of the temporal and energy widths. These extracted values are consistent with previous reports^{18, 20}. The positive sign of the covariance reflects the fact that, during emission of electrons from the quantum dot pump, later-ejected parts have higher energy than earlier-ejected parts^{20, 24}. As expected, the results of $\langle \Delta E_b^2 \rangle_g$ obtained using the hyperbolic tangent shaped waveform [blue rectangles in Fig. 3(c)] are consistent with those obtained using the sinusoidal waveform.

Our results demonstrate that, although the period of the detector barrier is large (~ 4 ns) and the time for the detectors to block the wave packet, $\sqrt{\langle \Delta E^2 \rangle_0} / \beta_b \sim 19$ ps, is insufficient to fully reconstruct the arrival time distribution¹⁹ of incident electrons with a temporal width of ~ 17 ps, it is still possible to extract the temporal variance and the covariance between energy and time. We further demonstrate that this modulation method operates well at large f_b and in a different sample (see Supplementary Note 2). A large f_b is useful for achieving a wide range of β_b for a given V_{AC} .

We visualize the Wigner distribution of incident electrons in Fig. 3(d), assuming that incident electrons are represented by a bivariate Gaussian Wigner distribution. This distribution well describes the behavior of the generated hot electrons observed experimentally²⁰, and can be characterized by the three extracted parameters (the temporal variance, covariance between energy and time, and energy variance). Comparison of the Wigner distribution in Fig. 3(d) with

that reconstructed by the tomographic method shows overall agreement (see Supplementary Note 3). We note that our measurement method is similar to methods in Ref. [17, 27, 28], where the Wigner distribution is reconstructed without complete tomographic reconstructions, by relying on the specific form of incident electrons. In contrast, our method does not assume any specific form for generated electrons.

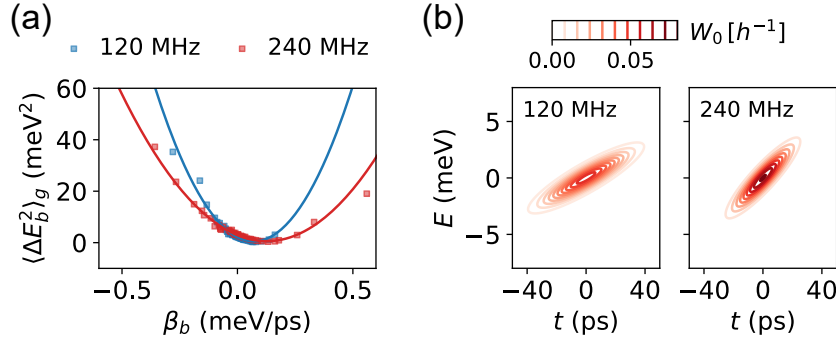


Figure 4. Measurements with trapezoidal pumping at $f_p = 120$ MHz and $f_p = 240$ MHz. (a) The barrier height variance $\langle \Delta E_b^2 \rangle_g$ obtained from g_b with the hyperbolic tangent waveform applied to the detector, is shown in blue ($f_p = 120$ MHz) and red ($f_p = 240$ MHz). The detector barrier frequencies are $f_b = 480$ MHz for $f_p = 120$ MHz and $f_b = 960$ MHz for $f_p = 240$ MHz. The solid lines represent fits to Eq. (2). (b) Wigner distributions of the generated electrons, assuming they follow a bivariate Gaussian Wigner distribution with the parameters obtained in (a).

We now generate electrons while applying a trapezoidal waveform to the quantum dot. Under this trapezoidal waveform, electrons will experience a linearly varying potential, insensitive to emission timing. We vary the pumping frequency f_p , which in turn modifies the emission distribution^{20, 29, 30}. Our time-resolved measurement method verifies these variations using extracted parameters. Figure 4(a) shows the barrier height variance $\langle \Delta E_b^2 \rangle_g$ obtained using trapezoidal pumping at 120 MHz (blue square) and 240 MHz (red square). We extract the temporal variance, covariance between energy and time, and energy variance from Eq. (2), as was done in Fig. 3. For pumping at 120 MHz, we obtain $\langle \Delta t^2 \rangle_0 = (18.1 \text{ ps})^2$, $\langle Et \rangle_0 - \langle E \rangle_0 \langle t \rangle_0 = 23.0 \text{ meV} \cdot \text{ps}$, and $\langle \Delta E^2 \rangle_0 \simeq (1.44 \text{ meV})^2$. For pumping at 240 MHz, we obtain $\langle \Delta t^2 \rangle_0 = (12.1 \text{ ps})^2$, $\langle Et \rangle_0 - \langle E \rangle_0 \langle t \rangle_0 = 18.4 \text{ meV} \cdot \text{ps}$, and $\langle \Delta E^2 \rangle_0 \simeq (1.70 \text{ meV})^2$. In extracting parameters, we exclude the four data points with the largest β_b values, to minimize

fluctuation errors at large $\langle \Delta E_b^2 \rangle_g$ values. The Wigner distributions of generated electrons, obtained assuming that they follow bivariate Wigner distributions, are shown in Fig. 4(b) (see Supplementary Note 3 for a detailed comparison with tomographic measurements). As the pumping frequency f_p increases, electron emission from the quantum dot to the quantum Hall channel occur on a shorter timescale, leading to a smaller temporal variance $\langle \Delta t^2 \rangle_0$ of the generated electrons. Because the quantum dot undergoes rapid energy variation during emission, the energy variance $\langle \Delta E^2 \rangle_0$ becomes large. Our results in Fig. 4 confirm this trend. This systematic study demonstrates the broad operability of our time-resolved measurements.

Discussion

We have demonstrated a method for extracting the temporal variance and the covariance between energy and time of incident electrons by applying a sinusoidal or hyperbolic tangent waveform to a detector potential barrier. By measuring the variance in the transconductance barrier height, we can determine these key parameters. The energy variance is obtained from measurements at a static barrier, enabling us to estimate the states of incident electrons. In this study, we estimate the energy variance of the electrons under the assumption that the energy scale of the detector is negligible. We believe that multiple barriers could be utilized to further separate the energy scales of incident electrons and the detector barrier.

Our method enables time-resolved measurements without requiring high-bandwidth RF signals, precise knowledge of the detector barrier shape, or the exact form of the incident electron wave packet. Importantly, the accuracy of parameter extraction in our method is not constrained by the barrier height ramping rate β_b . To identify parameters, our approach only requires that the variation in energy variance within transconductance, over a given range of β_b , is detectable within the energy resolution by the barrier. For $\beta_b \sim 0.1$ meV/ps, achieved in our experiment, electron temporal widths on the order of a few picoseconds can be resolved within our energy resolution. Increasing β_b is expected to improve parameter identification, enabling access to sub-picosecond time scales.

We assess the accuracy and potential sources of error in our approach. The uncertainty in extracted parameters is determined by evaluating confident intervals, where experimental data aligns with theoretical expectations (see Method). In our study, this uncertainty is found to be less than 4%, demonstrating the robustness of our extracted values. Another potential source

of error arises from fluctuations in the gate conversion factor. This effect, however, is negligible when the energy of electrons significantly exceeds the Fermi energy, where screening by bulk electrons is minimized³¹. In our study, the energy difference between the curves for electrons with and without LO phonon emission is nearly identical within a range of 90 meV [see Fig. 3(a)], indicating that errors due to fluctuations in the gate conversion factor are negligible. We use Gaussian curve fitting to extract the variance of the barrier height in transconductance, as this approach accurately represents the measured data in the presence of noise. Our method can be applied to electron wave packets of arbitrary shape by manually computing the variance through integration over finite regions of the transconductance.

Our approach can be used with both sinusoidal and trapezoidal waveforms applied to the detector barrier. Our results demonstrate that the sinusoidal waveform is more time-efficient and accurate, as it eliminates the need to vary the ramping speed and avoids additional errors introduced by synthesizing the waveform with higher harmonics. We perform measurements for electrons obtained using trapezoidal waveform pumping while varying the pumping frequency. Our results show that the extracted parameters are consistent with expectations, as a result of varying pumping conditions. We estimate that the proposed measurement method will be useful for efficiently examining quantum states of incident electrons and will be valuable in electron quantum optics and quantum information processing.

Methods

Sample fabrication and measurement

The GaAs/AlGaAs device is fabricated with the top-gate electrodes, as shown in Fig. 1a. A 2DEG is generated at a depth of 70 nm beneath the surface. The carrier density and mobility are $\sim 2.5 \times 10^{11} \text{ cm}^{-2}$ and $\sim 70 \text{ m}^2 \text{ V}^{-1} \text{ s}^{-1}$, respectively. The device is cooled below 420 mK. The electric current is measured at a terminal positioned across the barrier using an ammeter, which consists of an I/V converter-type current amplifier with a gain of 10^9 and a digital voltmeter. A Tektronix AWG7122C arbitrary waveform generator (AWG) is used to generate the waveforms for both pumping and detection in Figs. 3 and 4. This AWG is also used for tomographic measurements (see Supplementary Note 3).

Parameter extraction from the transconductance

The rate β_b is obtained from the slope of the finite-value region in the transconductance. The value of $\langle \Delta E_b^2 \rangle_g$ is obtained by fitting a Gaussian curve to the cross-sectional profile of the transconductance g_b along the barrier height E_b , as the Gaussian function accurately describes the shape of g_b . The extraction is performed using Lmfit, an open-source software package in Python³². It optimizes parameters via the least-squares method by minimizing the chi-square value, which quantifies the weighted sum of squared differences between the experimental data and the model.

To extract the parameters of temporal variance, energy-time covariance, and energy variance along with their standard errors, we also use Lmfit by comparing the obtained $\langle \Delta E_b^2 \rangle_g$ with Eq. (2). The standard errors of the extracted parameters, determined by the range of values, where the change in chi-square becomes significant, is less than 4% in the extractions shown in Figs. 3 and 4.

Data availability

The data supporting the findings of this study are available upon request.

Code availability

The theoretical results of the manuscript are reproducible, as demonstrated in Supplementary Note 1. Additional code is available upon request.

Acknowledgement

This work was supported by the National Research Foundation funded by the Korean Government (Grant Nos. RS-2023-00207732, RS-2021-NR059826, RS-2023-00256050, and RS-2023-00283291, RS-2024-00463743). This research was also partially supported by Development of quantum-based measurement technologies funded by Korea Research Institute of Standards and Science (KRISS-2025-GP2025-0010). This research was partially supported by Global - Learning & Academic research institution for Master's·PhD students, and Postdocs

(LAMP) Program of the National Research Foundation of Korea (NRF) grant funded by the Ministry of Education (RS-2024-00443714).

Author contributions

W.P. and M.H.B. conceived the study. H.K.C provided GaAs/AlGaAs wafers. M.H.B, B.K.K. and W.P. designed devices. B.K.K. fabricated the devices and measured the carrier density and mobility of the wafer at $T = 2$ K. C.Y. performed the measurements, assisted by Y.S.K. and B.K.K.. W.P. developed the analytical model and analyzed data. The manuscript was mainly written by W.P. with review by other authors. All authors contributed to the discussion of results.

Competing interests

The authors declare no competing interests.

References

1. Fève G, *et al.* An on-demand coherent single-electron source. *Science* **316**, 1169-1172 (2007).
2. Dubois J, *et al.* Minimal-excitation states for electron quantum optics using levitons. *Nature* **502**, 659-663 (2013).
3. Assouline A, *et al.* Emission and coherent control of Levitons in graphene. *Science* **382**, 1260-1264 (2023).
4. Blumenthal MD, *et al.* Gigahertz quantized charge pumping. *Nature Physics* **3**, 343-347 (2007).
5. Giblin SP, *et al.* Towards a quantum representation of the ampere using single electron pumps. *Nature communications* **3**, 930 (2012).
6. Yamahata G, Nishiguchi K, Fujiwara A. Gigahertz single-trap electron pumps in silicon. *Nature communications* **5**, 5038 (2014).
7. Kaestner B, Kashcheyevs V. Non-adiabatic quantized charge pumping with tunable-

- barrier quantum dots: a review of current progress. *Reports on Progress in Physics* **78**, 103901 (2015).
8. McNeil RPG, *et al.* On-demand single-electron transfer between distant quantum dots. *Nature* **477**, 439-442 (2011).
 9. Hermelin S, *et al.* Electrons surfing on a sound wave as a platform for quantum optics with flying electrons. *Nature* **477**, 435-438 (2011).
 10. Bocquillon E, *et al.* Electron quantum optics: partitioning electrons one by one. *Physical Review Letters* **108**, 196803 (2012).
 11. Bocquillon E, *et al.* Coherence and indistinguishability of single electrons emitted by independent sources. *Science* **339**, 1054-1057 (2013).
 12. Bäuerle C, *et al.* Coherent control of single electrons: a review of current progress. *Reports on Progress in Physics* **81**, 056503 (2018).
 13. Edlbauer H, *et al.* Semiconductor-based electron flying qubits: review on recent progress accelerated by numerical modelling. *EPJ Quantum Technology* **9**, 21 (2022).
 14. Grenier C, *et al.* Single-electron quantum tomography in quantum Hall edge channels. *New Journal of Physics* **13**, 093007 (2011).
 15. Jullien T, Roulleau P, Roche B, Cavanna A, Jin Y, Glattli DC. Quantum tomography of an electron. *Nature* **514**, 603-607 (2014).
 16. Bisognin REMI, *et al.* Quantum tomography of electrical currents. *Nature Communications* **10**, 3379 (2019).
 17. Fletcher JD, *et al.* Clock-controlled emission of single-electron wave packets in a solid-state circuit. *Physical Review Letters* **111**, 216807 (2013).
 18. Waldie J, *et al.* Measurement and control of electron wave packets from a single-electron source. *Physical Review B* **92**, 125305 (2015).
 19. Park W, Sim H-S, Ryu S. Measuring the arrival time of an electron wave packet using a dynamical potential barrier. *Physical Review B* **108**, 195309 (2023).
 20. Fletcher JD, *et al.* Continuous-variable tomography of solitary electrons. *Nature communications* **10**, 5298 (2019).

21. Locane E, Brouwer PW, Kashcheyevs V. Time-energy filtering of single electrons in ballistic waveguides. *New Journal of Physics* **21**, 093042 (2019).
22. Kim M-S, *et al.* Tailoring Single-Electron Emission Distributions in the Time–Energy Phase Space. *Nano Letters* **24**, 13140-13146 (2024).
23. Case WB. Wigner functions and Weyl transforms for pedestrians. *American Journal of Physics* **76**, 937-946 (2008).
24. Kataoka M, Fletcher JD, Johnson N. Time-resolved single-electron wave-packet detection. *physica status solidi (b)* **254**, 1600547 (2017).
25. Johnson N, *et al.* LO-phonon emission rate of hot electrons from an on-demand single-electron source in a GaAs/AlGaAs heterostructure. *Physical Review Letters* **121**, 137703 (2018).
26. Taubert D, *et al.* Relaxation of hot electrons in a degenerate two-dimensional electron system: transition to one-dimensional scattering. *Physical Review B* **83**, 235404 (2011).
27. Fletcher JD, *et al.* Coulomb sensing of single ballistic electrons. *arXiv preprint arXiv:241215789*, (2024).
28. Fletcher JD, *et al.* Time-resolved Coulomb collision of single electrons. *Nature Nanotechnology* **18**, 727-732 (2023).
29. Ryu S, Kataoka M, Sim H-S. Ultrafast emission and detection of a single-electron Gaussian wave packet: a theoretical study. *Physical Review Letters* **117**, 146802 (2016).
30. Kashcheyevs V, Samuelsson P. Classical-to-quantum crossover in electron on-demand emission. *Physical Review B* **95**, 245424 (2017).
31. Kim B-K, Ghee Y-S, Park W, Park S-I, Song J, Bae M-H. Extension of quantized-current plateaus in tunable-barrier single-electron pumps through charge screening of the electrostatic field. *AIP Advances* **14**, (2024).
32. Newville M, Stensitzki T, Allen DB, Rawlik M, Ingargiola A, Nelson A. LMFIT: Non-linear least-square minimization and curve-fitting for Python. *Astrophysics Source Code Library*, ascl: 1606.1014 (2016).

Supplementary Information for

**Time-resolved measurement of single electrons
using a modulated barrier**

Wanki Park^{1*†}, Chanuk Yang^{2,3†}, Young-Seok Ghee¹, Hyung Kook Choi³, Bum-Kyu Kim¹ and Myung-Ho Bae^{1,4*}

¹Korea Research Institute of Standards and Science, Daejeon 34113, Republic of Korea

²Jeonbuk National University G-LAMP Project Group, Jeonbuk National University, Jeonju 54896, Republic of Korea

³Department of Physics, Jeonbuk National University, Jeonju 54896, Republic of Korea

⁴KAIST Graduate School of Quantum Science and Technology, Korea Advanced Institute of Science and Technology, Daejeon 34141, Republic of Korea

[†]W.P. and C.Y. contributed equally to this work.

*e-mail: wanki@kriss.re.kr, mhbae@kriss.re.kr

Contents

Supplementary Note 1: Derivation of Eq. (2) of the main text

Supplementary Note 2: Time-resolved measurement for different sample

Supplementary Note 3: Tomographic reconstruction

Supplementary References

Supplementary Note 1. Derivation of Eq. (2) of the main text

We present a detailed derivation of Eq. (2) from Eq. (1), introduced in the main text. The transconductance of Eq. (1) can be expressed in convolution form as

$$g_b = -\frac{\partial}{\partial E_b} \int_{-\infty}^{\infty} dt \int_{-\infty}^{\infty} dE W_0(E, t) T(E - E_b - \beta_b t + \text{const}) \quad (\text{S1})$$

$$= \int_{-\infty}^{\infty} dE \underbrace{\int_{-\infty}^{\infty} dt W_0(E + \beta_b t - \text{const}, t)}_{f(E)} \underbrace{\left[-\frac{\partial}{\partial E_b} T(E - E_b) \right]}_{h(E_b - E)} \quad (\text{S2})$$

$$= \int_{-\infty}^{\infty} dE f(E) h(E_b - E) \quad (\text{S3})$$

We note that the integral of either function f or h over the energy (barrier height) is 1. From the convolutional form of g_b [Eq. (S3)], the variance in the barrier height is given by the sum of the variance of the functions f and h ,

$$\langle \Delta E_b^2 \rangle_g \equiv \int_{-\infty}^{\infty} dE_b E_b^2 g_b - \left[\int_{-\infty}^{\infty} dE_b E_b g_b \right]^2 \quad (\text{S4})$$

$$= \int_{-\infty}^{\infty} dE E^2 f - \left[\int_{-\infty}^{\infty} dE E f \right]^2 + \int_{-\infty}^{\infty} dE_b E_b^2 h - \left[\int_{-\infty}^{\infty} dE_b E_b h \right]^2. \quad (\text{S5})$$

From the definition of f in Eq. (S2), we obtain

$$\int_{-\infty}^{\infty} dE E^2 f - \left[\int_{-\infty}^{\infty} dE E f \right]^2 = \langle \Delta E^2 \rangle_0 - 2\beta_b [\langle Et \rangle_0 - \langle E \rangle_0 \langle t \rangle_0] + \beta_b^2 \langle \Delta t^2 \rangle_0, \quad (\text{S6})$$

where $\langle O \rangle_0 \equiv \int_{-\infty}^{\infty} dE dt O W_0$. Defining the square root of $\int_{-\infty}^{\infty} dE_b E_b^2 h - \left[\int_{-\infty}^{\infty} dE_b E_b h \right]^2$ as Δ_b , i.e., the energy width of $\partial T / \partial E$, and using Eqs. (S5) and (S6), we find that $\langle \Delta E_b^2 \rangle_g$ of Eq. (S4) corresponds to Eq. (2) in the main text.

Supplementary Note 2. Time-resolved measurement for different sample

We demonstrate our time-resolved measurement method on a different sample and at a higher detecting barrier frequency. In this demonstration, a Tektronix AWG7122C arbitrary waveform generator (AWG) is used to generate the pumping waveform, while a Keysight E8247C PSG continuous waveform generator (CWG) is used for detection.

As in Fig. 3(c) of the main text, Fig. S1(a) shows the barrier height variance $\langle \Delta E_b^2 \rangle_g$ at a

pumping frequency $f_p = 960$ MHz and a detecting barrier frequency $f_b = 960$ MHz. The sinusoidal wave is used for both pumping and detecting. The data is well-fitted to Eq. (2) of the main text (black solid curve). From this fit, we extract $\langle \Delta t^2 \rangle_0 = (12.9 \text{ ps})^2$ and $\langle Et \rangle_0 - \langle E \rangle_0 \langle t \rangle_0 = 18.1 \text{ meV} \cdot \text{ps}$. From the value $\langle \Delta E_b^2 \rangle_g$ at $\beta_b = 0$, we obtain the energy variance $\langle \Delta E^2 \rangle_0 \simeq (2.9 \text{ meV})^2$. The extracted $\langle \Delta E^2 \rangle_0$ is much larger than that reported in previous studies^{S1, S2}, indicating the presence of additional noise in this sample.

Assuming that generated electrons are described by a bivariate Gaussian form, the Wigner distribution of incident electrons is visualized in Fig. S1(b). The detector frequency of $f_b = 960$ MHz is larger than 240 MHz used in Fig. 3 of the main text. This large f_b allows for a wide range of β_b for a given V_{AC} . The period $1/f_b \sim 1000$ ps is sufficiently long compared to the temporal width ~ 13 ps of the incident electrons. Thus, in our experimental regime, the barrier height rate β_b can be approximated as linear during the traversal of electrons through the detector, and Eq. (2) of the main text remains valid.

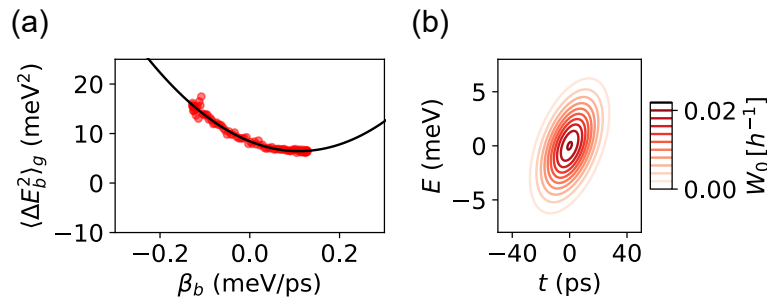


Figure S1. Results at a pumping frequency $f_p = 960$ MHz, detecting barrier frequency $f_b = 960$ MHz, $V_{AC} = 40$ mV, and $\alpha_b = 0.52$ eV/V (α_b deduced from LO phonon emissions). (a) The barrier height variance $\langle \Delta E_b^2 \rangle_g$ obtained using a sinusoidal wave on the detector is shown as the red circles, fitted to Eq. (2) of the main text (the black solid curve). (b) A Wigner distribution W_0 of incident electrons is shown, assuming that incident electrons follow a bivariate Gaussian Wigner distribution with the parameters obtained in (a).

Supplementary Note 3. Tomographic reconstruction

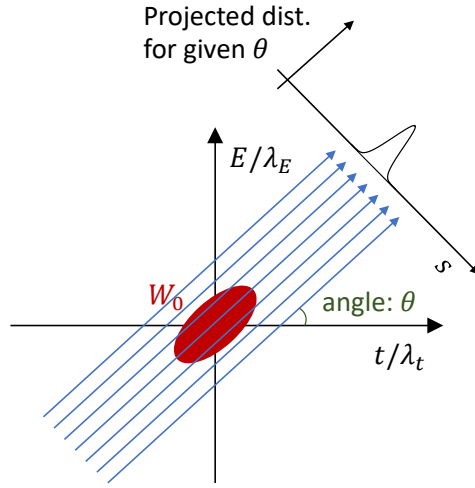


Figure S2. The Wigner distribution W_0 (red oval) projected along the line (blue arrows) at an angle θ . The projected distribution for given θ is shown as the black curve in the upper right panel. λ_t and λ_E are normalized values used to make quantities dimensionless.

We show tomographic results (corresponding to incident electrons used in Figs. 3 and 4 of the main text) and compare them with those obtained using extracted parameters, assuming a bivariate Wigner distribution.

We employ the tomographic method to reconstruct the Wigner distribution as in Fletcher et al.^{S1} and Kim et al.^{S3}. We first outline the transformation method that is similar to the computed tomography method, as schematically shown in Fig. S2. Our target to reconstruct is a Wigner distribution W_0 (denoted in time-energy phase space, shown as the red oval). We achieve this by projecting the Wigner distribution (see below for the experimental method) with an angle θ along the s axis (upper right panel), which is perpendicular to the projection lines (blue arrows). By collecting the projected distributions while varying θ , we obtain a sinogram, which is the Radon-transformed data of the target. Using the inverse Radon transformation, we finally obtain the target of the Wigner distribution.

We review the detailed experimental method to obtain the projected distribution and the sinogram^{S1, S3}. The projected distribution can be obtained by measuring a transmitted current I_T through the detector barrier at a rate β_b . For a linearly time-varying potential (a hyperbolic tangent shape is typically used as implemented in the experiment and described in the main text), the transmission probability P_T (the normalized value of I_T with pumping current ef) follows^{S4}

$$P_T = \int_{-\infty}^{\infty} dt \int_{-\infty}^{\infty} dE W_0(E, t) T(E - E_b - \beta_b(t - t_d)), \quad (\text{S7})$$

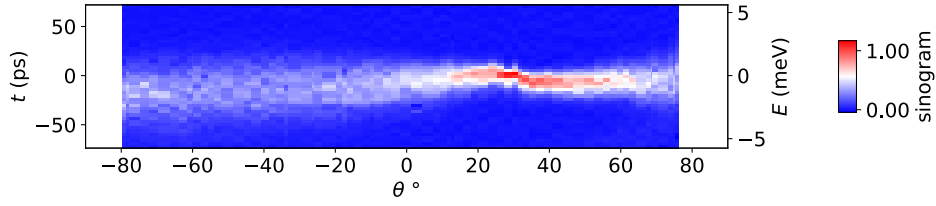
where T represents the transmission probability of a monochromatic wave through the barrier. E_b and t_d denote the DC barrier height and time delay of the detector barrier, respectively. When the energy width of dT/dE is negligible compared to the energy scale of W_0 , T can be approximated as a step function. In this case, the derivative of P_T provides the projected distribution along a given derivative direction. The finite width of dT/dE gives an error in measurement^{S4}. To make phase-space coordinate dimensionless, we introduce the normalized parameters, λ_E ($E \rightarrow E/\lambda_E$ and $E_b \rightarrow E_b/\lambda_E$) and λ_t ($t \rightarrow t/\lambda_t$). In this coordinate, the projection angle θ is related to the rate β_b by $\theta = \tan^{-1}(\beta_b/\beta_0)$, where $\beta_0 = \lambda_E/\lambda_t$. β_0 is empirically chosen in the experiment based on the applied gate voltage on the detector. As in Ref. [S1], we use a hyperbolic tangent waveform to the detector,

$$V_b(t) = V_{AC} \tanh[A_0 \tan \theta \sin[2\pi f_b(t - t_d)]] + V_{DC}. \quad (\text{S8})$$

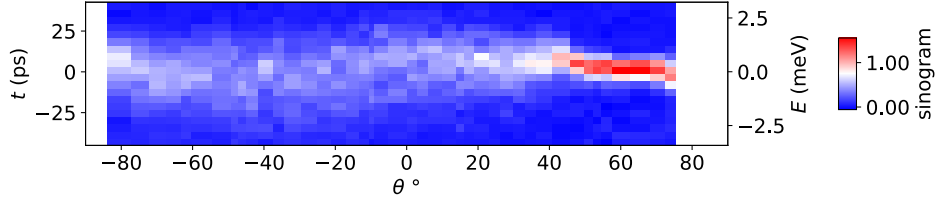
In this waveform, β_0 is determined by A_0 , V_{AC} , and gate conversion factor.

By collecting the projected distribution ($\approx dP_T/ds$) (s is the coordinate perpendicular to the projection lines, see Fig. S2) while varying the projection angle θ , barrier height E_b , and time delay t_d , we obtain the sinogram (Fig. S3). Due to experimental limitations, the projection angles above 85° or below -85° cannot be reached. This limitation may arise from the finite bandwidth of AWG or signal damping at large β_b . Using the inverse Radon transformation (implemented via `iradon` function in `skimage` python library) and reverting the dimensionless coordinate back to their dimensional form, we reconstruct the Wigner distribution (Fig. S4). The tomographic results correspond to the measurement shown in Figs. 3 and 4 of the main text.

(a) Sinogram for Fig. 3



(b) Sinogram for 120MHz in Fig. 4



(c) Sinogram for 240MHz in Fig. 4

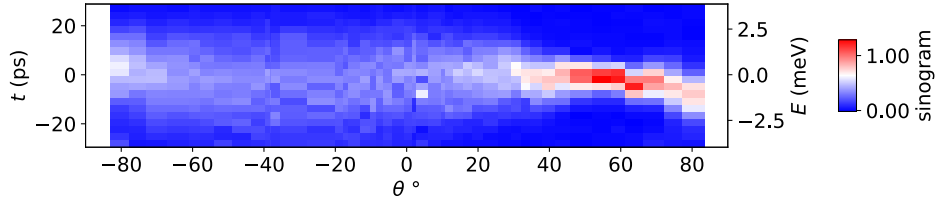


Figure S3. Sinograms as a function of the projection angle θ and the dimensionless coordinate s . The corresponding time axis (for $\theta = 90^\circ$, where the sinogram represents the arrival time distribution) and energy axis (for $\theta = 0^\circ$, where the sinogram represents the energy distribution) are shown in the plot. The sinograms are obtained for the generated electrons under the conditions of (a) Fig. 3 and (b, c) Fig. 4, with a pumping frequency of (b) 120 MHz and (c) 240 MHz, as described in the main text. In (a) and (c), $\beta_0 = 0.09$ meV/ps is used, while in (b), $\beta_0 = 0.05$ meV/ps is used.

We now analyze the tomographic results (right panels of Fig. S4) and compare them with the results obtained by assuming a bivariate Wigner distribution with extracted parameters from the main text (the left side of the left panels of Fig. S4). To independently evaluate errors caused by the limited range of tomographic angle, we compute the sinogram of the bivariate Wigner distributions using the same tomographic angles and the same range of s coordinate as in the experimental tomographic reconstruction. The inverse Radon-transformed result, accounting for these errors, is shown in the right side of the left panels of Fig. S4.

We found overall agreement between the tomographic reconstruction results and the results obtained from the bivariate Wigner distribution using the extracted parameters in the main text. The results support our time-resolved measurements utilizing a barrier height variance of the

transconductance. Reconstruction errors arise from the limited range of tomographic angles and the presence of noises, which we estimate, particularly higher at higher values of β_b .

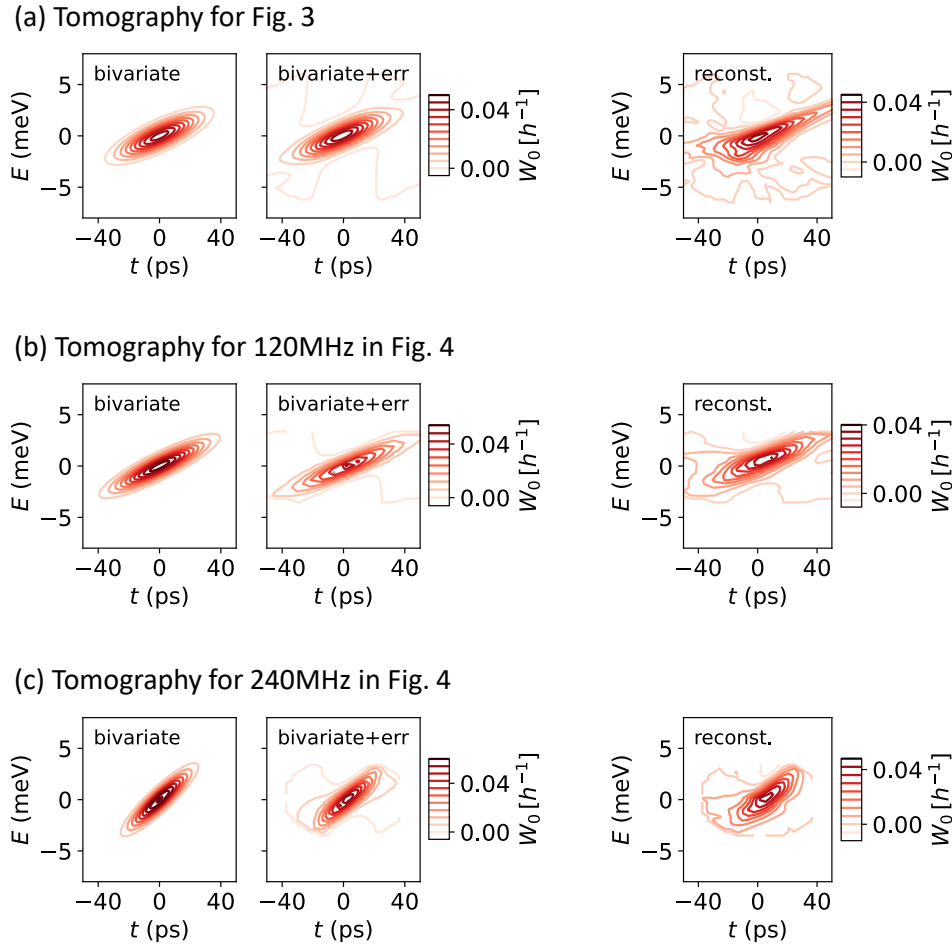


Figure S4. Wigner distribution of generated electrons in the time-energy phase space. The right panels show the results obtained through the tomographic procedure (see sinogram in Fig. S3). The left panels present the bivariate Wigner distributions with the parameters obtained in the main text. The middle panels account for errors due to a finite tomographic angle in the right panel (see the text for detail). The results correspond to the generated electrons under the conditions of (a) Fig. 3 and (b, c) Fig. 4 of the main text. For (b) and (c), the pumping frequency are 120 MHz and 240 MHz, respectively.

Supplementary references

- S1. Fletcher JD, *et al.* Continuous-variable tomography of solitary electrons. *Nature communications* **10**, 5298 (2019).

- S2. Waldie J, *et al.* Measurement and control of electron wave packets from a single-electron source. *Physical Review B* **92**, 125305 (2015).
- S3. Kim M-S, *et al.* Tailoring Single-Electron Emission Distributions in the Time–Energy Phase Space. *Nano Letters* **24**, 13140-13146 (2024).
- S4. Locane E, Brouwer PW, Kashcheyevs V. Time-energy filtering of single electrons in ballistic waveguides. *New Journal of Physics* **21**, 093042 (2019).